Ba et al.
Chinese Journal of Mechanical Engineering (2024) 37:27
https://doi.org/10.1186/s10033-023-00988-1

Chinese Journal of Mechanical Engineering

ORIGINAL ARTICLE

Open Access

Force Compensation Control for Electro-Hydraulic Servo System with Pump–Valve Compound Drive via QFT–DTOC

Kaixian Ba[1,2], Yuan Wang[2], Xiaolong He[2], Chunyu Wang[2], Bin Yu[1,2,3*], Yaliang Liu[2] and Xiangdong Kong[1,2,3]

Abstract

Each joint of a hydraulic-driven legged robot adopts a highly integrated hydraulic drive unit (HDU), which features a high power–weight ratio. However, most HDUs are throttling-valve-controlled cylinder systems, which exhibit high energy losses. By contrast, pump control systems offer a high efficiency. Nevertheless, their response ability is unsatisfactory. To fully utilize the advantages of pump and valve control systems, in this study, a new type of pump–valve compound drive system (PCDS) is designed, which can not only effectively reduce the energy loss, but can also ensure the response speed and response accuracy of the HDUs in robot joints to satisfy the performance requirements of robots. Herein, considering the force control requirements of energy conservation, high precision, and fast response of the robot joint HDU, a nonlinear mathematical model of the PCDS force control system is first introduced. In addition, pressure–flow nonlinearity, friction nonlinearity, load complexity and variability, and other factors affecting the system are considered, and a novel force control method based on quantitative feedback theory (QFT) and a disturbance torque observer (DTO) is designed, which is denoted as QFT–DTOC herein. This method improves the control accuracy and robustness of the force control system, reduces the effect of the disturbance torque on the control performance of the servo motor, and improves the overall force control performance of the system. Finally, experimental verification is performed using the PCDS performance test platform. The experimental results and quantitative data show that the QFT–DTOC proposed herein can significantly improve the force control performance of the PCDS. The relevant force control method can be used as a bottom-control method for the hydraulic servo system to provide a foundation for implementing the top-level trajectory planning of the robot.

Keywords Legged robot, Pump–valve compound drive system (PCDS), Force compensation control, Quantitative feedback theory (QFT), Disturbance torque observer (DTO)

1 Introduction

In recent years, mobile robots have been increasingly used in various industries and investigated extensively. Based on the motion mode, robots can be classified into wheeled, crawler, legged, serpentine, and spherical robots [1–5]. In contrast with other types of robots, legged bionic robots offer noncontinuous support and good adaptability to unknown and complex environments. In recent years, bionic legged robots combined with hydraulic drives have been implemented to replace

*Correspondence:
Bin Yu
yb@ysu.edu.cn
[1]Hebei Provincial Key Laboratory of Heavy Machinery Fluid Power Transmission and Control, Qinhuangdao 066004, China.
[2]School of Mechanical Engineering, Yanshan University, Qinhuangdao 066004, China.
[3]National Engineering Research Center for Local Joint of Advanced Manufacturing Technology and Equipment, Yanshan University, Qinhuangdao 066004, China.

human beings to perform detection, transportation, rescue, military assistance, and other tasks in a complex environment. These robots feature a high power-to-weight ratio, a large loading capacity, and fast response; they are widely used in military and civilian applications.

Currently, a highly integrated electro-hydraulic servo system is primarily adopted in the leg joint drivers of advanced hydraulic-driven legged robots. The typically used electro-hydraulic servo system is available two forms: the valve-controlled cylinder system [6–8] and pump-controlled cylinder system [9, 10]. The valve-controlled cylinder system is controlled using an electro-hydraulic servo valve. Meanwhile, for the pump-controlled cylinder system, the output flow and pressure of the pump are matched with the load requirements by changing the position or speed of the pump. The valve-controlled cylinder system is a throttle system that features high energy loss. Moreover, the different pressure or flow requirements of each joint of the robot will cause a significant energy loss and reduce the endurance of the legged robots. The pump-controlled cylinder system is a direct-drive system. Although it features a higher energy efficiency than that of the valve-controlled cylinder system, its response speed and control accuracy are lower. Therefore, to overcome the shortcomings of the two systems when they are used alone and to combine their respective advantages, an electro-hydraulic servo system with fast response, high precision, and low energy loss must be designed.

Both force and position control are important bottom-control methods in robot control systems. In recent years, hydraulic and motor force control systems have been investigated extensively, and various control methods have been adopted, such as fuzzy logic control [11–14], sliding mode control [15, 16], robust control [17, 18], and intelligent control [19–22]. The optimization of the control performance of force control systems has been demonstrated previously. However, in the practical application of robot systems, to ensure the stability of the body, algorithms of the core controller based on PID are still necessitated [23–25]. In particular, an electrohydraulic servo system with a pump–valve compound drive, known as a pump–valve compound drive system (PCDS), features a fast response, high precision, and high energy utilization. However, when the system is disrupted by a complex and changeable external position, the high-performance force control requirements of the robot system will be difficult to satisfy. In addition, the hydraulic actuator of the system exhibits an asymmetric cylinder structure, and a few problems arise, such as the inconsistency of forward and negative dynamic characteristics; therefore, its control accuracy and robustness must be improved.

Based on a previous study as a foundation [26], the authors performed a mathematical modeling and parameter sensitivity analysis of the valve-controlled cylinder force control system and discovered the effects of the parameters in the system on the force control performance, thus providing a foundation for the optimization of the mathematical model. In addition, a force-control-performance optimization algorithm for force-based impedance control was investigated, and a compliance-eliminated controller was designed to improve the disturbance rejection performance of a valve-controlled cylinder force control system [27]. Consequently, a preliminary basis was provided for mathematical modeling, system design, and control algorithm research.

This study is performed as follows: First, a nonlinear mathematical model of the PCDS force closed-loop control system is constructed. Second, QFT–DTOC, a force-control method that combines quantitative feedback theory (QFT) and a disturbance torque observer (DTO), is designed to improve the control performance of the conventional PID controller. Finally, the effectiveness of the system performance and force control method is verified on the experimental platform of the PCDS, and the control effect is quantitatively analyzed.

2 Mathematical Model of PCDS Force Closed-Loop Control System

2.1 System Composition and Structure

A hydraulic schematic diagram of the PCDS force control performance test platform is shown in Figure 1; it is primarily composed of a position closed-loop control system and a tested PCDS force control system.

To satisfy the control performance requirements of the PCDS force control while providing energy conservation, fast response, and high precision, the system should comprise three closed-loop control systems: the force control system of the pump-controlled loop, the pressure control system of the asymmetrical cylinder rodless cavity, and the pressure control system of the asymmetric cylinder rod cavity. A schematic illustration of PCDS force control is shown in Figure 2.

2.2 System Mathematical Modeling

To investigate the force compensation control method of the PCDS, an overall mathematical model of PCDS force control was established based on Figure 2.

In particular, a mathematical model of the key components of the PCDS, including the servo motor, gear pump, filling loop, and asymmetrical cylinder, was established.

A mathematical model of the servo motor was constructed, and the voltage balance equation of the servo motor is as follows:

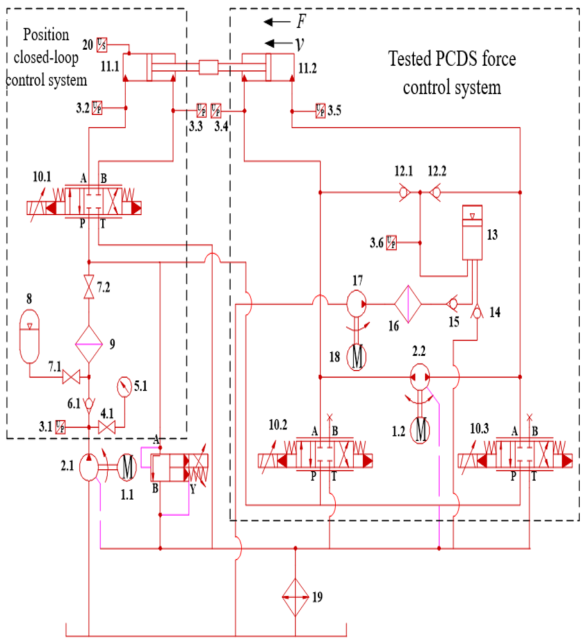

Figure 1 Hydraulic schematic diagram of PCDS force control performance test platform. 1-servo motor; 2-gear pump; 3-pressure sensor; 4-pressure gauge switch; 5-pressure gauge; 6-check valve at pump outlet; 7-stop valve; 8-energy accumulator; 9-filter; 10-servo valve; 11-asymmetric cylinder; 12-check valve; 13-pressurized tank; 14-pressure release check valve; 15-oil replenishment check valve; 16-low pressure filter; 17-oil replenishment pump; 18-oil replenishment motor; 19- cooler; 20-position sensor

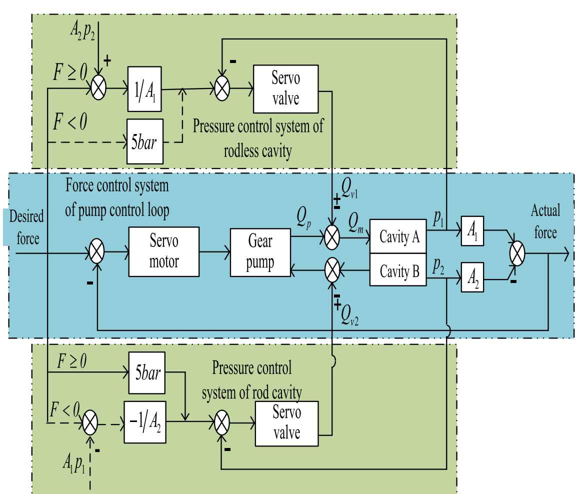

Figure 2 PCDS force closed-loop control block diagram

$$U_c = E + L\frac{di}{dt} + Ri, \tag{1}$$

where E is the back electromotive force, i the armature current, L the armature inductance, and R the armature winding resistance.

The reverse electromotive force of the servo motor is expressed as follows:

$$E = K_c w, \tag{2}$$

where K_c is the electromagnetic torque system, and w is the servo motor speed.

$$T_e = K_t i, \tag{3}$$

where K_t is the torque coefficient of the servo motor, and T_e the electromagnetic torque of the servo motor.

The servo motor and gear pump are directly connected, and the torque balance equation is as follows:

$$T_e = J\dot{w} + B_p w + T_L, \tag{4}$$

where J is the conversion of the moment of inertia of the servo motor shaft, B_p the viscous friction coefficient of the servo motor, and T_L the external load torque of the servo motor.

To control the servo motor accurately, three types of closed-loop control are typically used: current closed loop, speed closed loop, and position closed loop from inside to outside. The torque control of the servo motor adopts a current closed loop, and the dynamic response is rapid. This study primarily focuses on the force control of the PCDS and considers the response of the system; thus, the torque control mode is adopted in the servo motor of the system. The current loop controller K_{PI} can set the control parameters of the current loop to accurately control the servo motor torque. The transmission block diagram of the servo motor torque control system is shown in Figure 3.

In Figure 3, K_V represents a voltage and current conversion system, where the effect of the external interference torque of the servo motor is disregarded. The open-loop transfer function between the input voltage and the output speed of the servo motor is expressed as follows:

$$\frac{w}{U} = \frac{K_J K_{PI} K_t}{LJ^2 s^3 + RJ^2 s^2 + J(K_c K_t + K_{PI} K_f)s}. \tag{5}$$

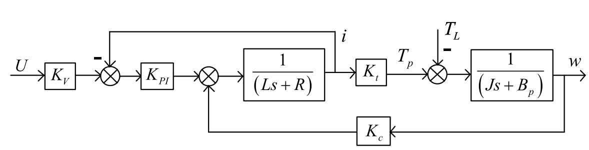

Figure 3 Transmission block diagram of servo motor torque control system

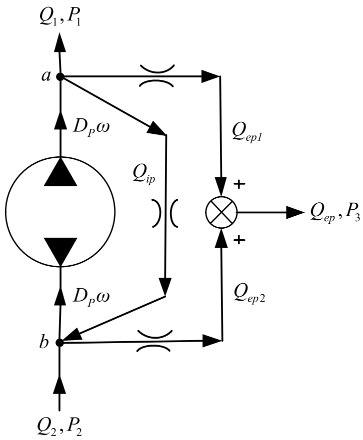

Figure 4 Diagram showing flow–pressure relationship of gear pump

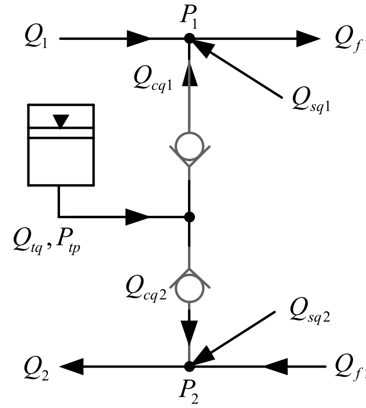

Figure 5 Diagram showing flow–pressure relationship between low pressure fuel tank and check valve oil replenishment

2.2.1 Mathematical Model Construction of Gear Pump

When the gear pump is propagating forward, considering the internal and external leakage of the gear pump, the flow–pressure relationship is as shown in Figure 4.

The flow equations of the gear pumps are as follows:

$$Q_1 = D_p w - Q_{ip} - Q_{ep1}, \tag{6}$$

$$Q_2 = D_p w - Q_{ip} - Q_{ep2}, \tag{7}$$

where D_p is the displacement of the gear pump, w the speed of the gear pump, Q_{ip} the internal leakage flow of the gear pump, Q_{ep1} the external leakage flow of the gear pump at point a, and Q_{ep2} the external leakage flow of the gear pump at point b.

Considering the nonlinear problems of leakage flow and pressure, the following expressions are derived:

$$Q_{ip} = K_{ip}(P_1 - P_2), \tag{8}$$

$$Q_{ep1} = K_{im}(P_1 - P_3), \tag{9}$$

$$Q_{ep2} = K_{im}(P_2 - P_3), \tag{10}$$

where K_{ip} is the internal leakage coefficient of the gear pump, K_{im} the external leakage coefficient of the gear pump, p_1 the pressure of the gear pump at point a, p_2 the pressure of the gear pump at point b, p_3 the pressure of the gear pump at point c (Pa), and 0 bar the pressure directly related to the external tank.

2.2.2 Mathematical Model Construction of Filling Loop

Mathematical models of a pressurized fuel tank and one-way valves were constructed in this study.

The PCDS is a closed system that requires oil to be replenished to the system through an oil-compensating loop composed of a fuel tank, check valve, and servo valve. Its main functions are as follows:

1) Maintain a constant pressure in the low-pressure cavity of the asymmetric cylinder, 2) supply the hydraulic oil leakage of the force control system, and 3) prevent cavitation problems caused by high-frequency vibrations of the system.

In the modeling of a conventional pump control system, the oil replenishment link is typically disregarded, which results in a certain deviation in the analysis results. Therefore, the relationship between the flow rate and pressure in this study was analyzed, as shown in Figure 5.

The flow equation of each link is as follows:

$$Q_{f1} = Q_1 + Q_{cq1} + Q_{sq1}, \tag{11}$$

$$Q_{f2} = Q_2 - Q_{cq2} - Q_{sq2}, \tag{12}$$

$$Q_{tq} = Q_{cq1} + Q_{cq2}, \tag{13}$$

where Q_{cq1} is the check valve flow connected to the asymmetrical cylinder rodless cavity, Q_{cq2} the check valve flow connected to the asymmetrical cylinder rod cavity, Q_{sq1} the servo valve flow connected to the asymmetrical cylinder rodless cavity, Q_{sq1} the servo valve flow connected to the asymmetrical cylinder rod cavity, and Q_{tq} the flow out from the pressurized fuel tank.

Considering the check valve as the throttle port model, the following expression can be obtained:

$$Q_{cq1} = \begin{cases} K_{cp}\sqrt{p_{tp} - p_1}, & p_{tp} \geq p_1 \\ 0, & p_{tp} < p_1 \end{cases}, \tag{14}$$

$$Q_{cq2} = \begin{cases} K_{cp}\sqrt{p_{tp}-p_2}, & p_{tp} \geq p_2 \\ 0, & p_{tp} < p_2 \end{cases}, \tag{15}$$

where p_{tp} is the output pressure of the pressurized fuel tank, and K_{cp} is the flow pressure coefficient of the check valve.

Owing to the complexity of modeling pressurized fuel tanks and the fact that pressurized fuel tanks and energy accumulators exhibit similar functions, the mathematical model of an energy accumulator was used in this study instead of that of a pressurized fuel tank. The input flow and output pressure of the supercharged fuel tank are correlated as follows:

$$p_{tp} = p_{gp}V_{gv}^{k} / \left[V_{gv} - \int q_{tp}\mathrm{d}t\right]^{k}, \tag{16}$$

where p_{gp} is the initial pressure of the pressurized fuel tank; V_{gv} is the initial volume of gas in the pressurized fuel tank; k is the polytropic index of nitrogen, which is generally 1.0–1.4.

2.2.3 Derive Flow Equations of Servo Valve

The servo valves installed on the two sides of the asymmetric cylinder replenish or drain oil from the two chambers of the asymmetric cylinder. The transfer function of the servo valve can be simplified to that of a second-order oscillation system. The transfer function of the servo valve in terms of the input voltage and displacement of the valve core is as follows:

$$\frac{X_v}{U_g} = \frac{K_a K_{xv}}{\frac{s^2}{\omega^2} + \frac{2\zeta}{\omega}s + 1}, \tag{17}$$

where K_a is the gain of the servo valve power amplifier, K_{xv} the gain of the servo valve, ζ the damping ratio of the servo valve, and ω the natural frequency of the servo valve.

To simplify calculation, the slide valve level of the servo valve was set to that of an ideal zero-opening four-way slide valve, and a flow equation for the four-way slide valve was derived. The flow of the asymmetrical cylindrical rodless cavity is expressed as follows:

$$Q_{sq1} = \begin{cases} K_d x_{v1}\sqrt{p_s - p_1}, & x_{v1} \geq 0 \\ K_d x_{v1}\sqrt{p_1 - p_0}, & x_{v1} < 0 \end{cases}. \tag{18}$$

The inlet flow rate of the servo valve connected to the rod cavity is expressed as

$$Q_{sq2} = \begin{cases} K_d x_{v2}\sqrt{p_s - p_2}, & x_{v2} \geq 0 \\ K_d x_{v2}\sqrt{p_2 - p_0}, & x_{v2} < 0 \end{cases}, \tag{19}$$

where K_d is the equivalent flow coefficient, x_{v1} the displacement of the servo valve connected to the rodless cavity of the asymmetric cylinder, x_{v2} the displacement of the servo valve connected to the rod cavity of the asymmetric cylinder, p_s the supply oil pressure of the servo valve, p_1 the pressure of the asymmetrical cylinder rodless cavity, p_2 the pressure of the asymmetrical cylinder rod cavity, and p_0 the return oil pressure of the system (0 bar).

The equivalent flow coefficient is expressed as follows:

$$K_d = C_d W\sqrt{\frac{2}{\rho}}, \tag{20}$$

where C_d is the flow coefficient of the servo valve throttle orifice, W the area gradient, and ρ the hydraulic oil density.

2.2.4 Mathematical Model Construction of Asymmetrical Cylinder

(1) Derivation of Flow Continuity Equation The inlet flow of the asymmetrical cylinder rodless cavity and the oil-in-cavity volume are expressed as follows:

$$\begin{cases} Q_{f1} = A_1\frac{\mathrm{d}x_p}{\mathrm{d}t} + C_{im}(P_1 - P_2) + \frac{V_1}{\beta_e}\frac{\mathrm{d}p_1}{\mathrm{d}t} \\ V_1 = V_{01} + A_1 x_p \end{cases}. \tag{21}$$

The inlet flow of the asymmetrical cylinder rod cavity and the oil-out cavity volume are expressed as follows:

$$\begin{cases} Q_{f2} = A_2\frac{\mathrm{d}x_p}{\mathrm{d}t} + C_{im}(p_1 - p_2) + \frac{V_2}{\beta_e}\frac{\mathrm{d}p_2}{\mathrm{d}t} \\ V_2 = V_{02} - A_2 x_p \end{cases}, \tag{22}$$

where A_1 is the effective area of the asymmetrical cylinder rodless cavity, A_2 the effective area of the asymmetrical cylinder rod cavity, x_p the piston displacement of the asymmetrical cylinder, C_{im} the internal leakage coefficient of the asymmetrical cylinder, β_ε the elastic modulus of the effective volume, V_{01} the initial volume of the asymmetrical cylinder rodless cavity, and V_{02} the initial volume of the asymmetrical cylinder rod cavity.

The initial volumes of the rodless cavity and rod cavity of the asymmetric cylinder are expressed as follows, considering the volume variation of the operating cavity, connecting pipe, and asymmetric cylinder of the gear pump:

$$\begin{cases} V_{01} = V_{p1} + V_{g1} + A_1 L_0 \\ V_{02} = V_{p2} + V_{g2} + A_2(L - L_0) \end{cases}, \tag{23}$$

where V_{p1} is the volume of the operating cavity of the gear pump connected to an asymmetrical cylinder rodless cavity, V_{p2} the volume of the operating cavity of the gear pump connected to the asymmetrical cylinder rod

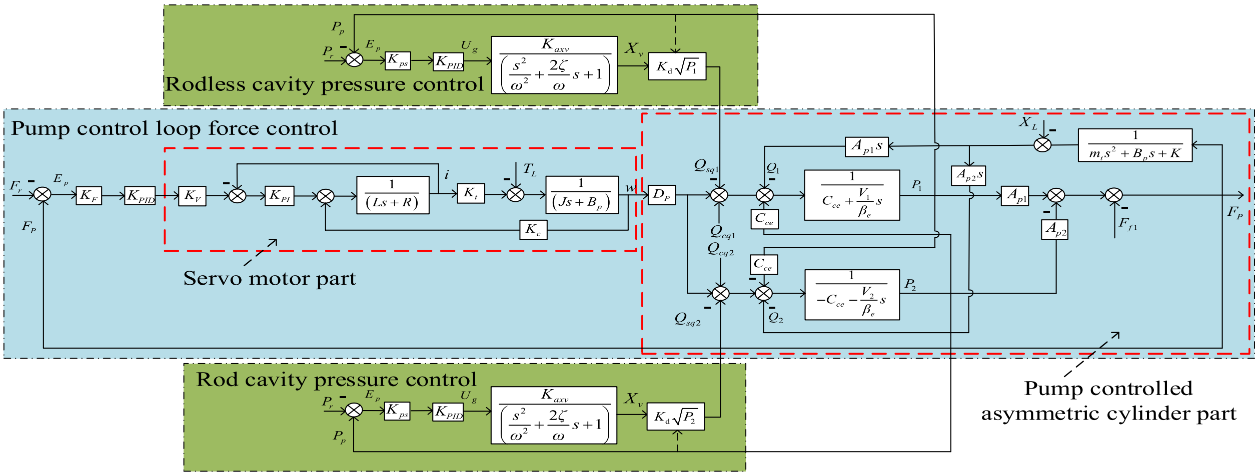

Figure 6 Overall mathematical model of PCDS force control

cavity, V_{g1} the pipe volume connected to the gear pump and the asymmetric cylinder rodless cavity, V_{g2} the pipe volume connected to the gear pump and the asymmetric cylinder rod cavity, L the total piston displacement of the asymmetrical cylinder, and L_0 the initial position of the asymmetrical cylinder.

(2) Derivation of Force Balance Equation Because the asymmetric cylinder is affected by the inertial force, viscous damping force, elastic force, and any external load force, the balance equations of the output and load forces of the asymmetric cylinder are derived as follows:

$$F_g = A_1 p_1 - A_2 p_2 = m_t \frac{\mathrm{d}x_p^2}{\mathrm{d}t} + B_p \frac{\mathrm{d}x_p}{\mathrm{d}t} + Kx_p + X_L + F_f, \tag{24}$$

where m_t is the total mass converted to the asymmetric cylinder piston, including the load mass block, piston, connection pipe, and oil in the asymmetric cylinder; K is the load stiffness of the asymmetric cylinder; B_p is the damping coefficient of the load and asymmetric cylinder; F_f is the Coulomb friction of the load and asymmetric cylinder; X_L is the arbitrary load location on the asymmetric cylinder piston.

2.2.5 Mathematical Model Construction of Pressure Sensor

The sampling frequency of the selected pressure sensor is more than five times that of the control system. The transfer function of the sensor is equivalent to a proportional link, and the transfer function between the feedback voltage and oil pressure is expressed as follows:

$$\frac{U_p}{P} = K_{ps}, \tag{25}$$

where K_{ps} is the gain of the pressure sensor, and P the pressure signal detected by the pressure sensor.

By combining Eqs. (1)–(25), the entire mathematical model of the PCDS force control can be established, in which a PID controller is adopted in the pump control and valve control loops, as shown in Figure 6.

2.3 Simplification of Transfer Function of Pump-controlled Asymmetric Cylinder

To facilitate the design of the pump control loop controller, the transfer function of the pump control loop was simplified without considering the effects of valve control and oil replenishment on the system. Additionally, the low-pressure cavity of the asymmetric cylinder was assumed to be zero.

The PCDS force-control transfer function is relatively complex and difficult to simplify. In addition, the difference between the forward and backward dynamic characteristics of the asymmetric cylinder was considered. Therefore, to facilitate the modeling, the asymmetric cylinder was modeled separately based on the positive and negative motions of the piston rod, and different proportional gains were used to reduce or eliminate the difference. In the positive motion of the piston rod of the asymmetric cylinder, the gear pump absorbs hydraulic oil from the rod cavity to output high pressure oil to the rodless cavity; its positive and negative motions are illustrated in Figure 7.

When the pump-controlled asymmetric cylinder is undergoing positive motion, its transfer function is derived as follows. The flow of the gear-pump high-pressure cavity is expressed as

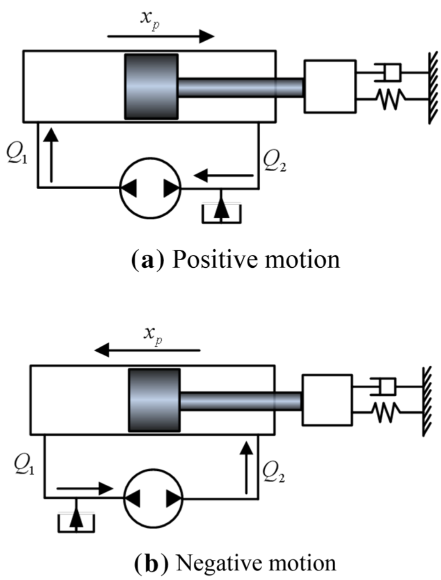

Figure 7 Diagrams illustrating positive and negative motions of pump-controlled asymmetric cylinder

$$Q_1 = D_p w - K_{ip} p_1. \tag{26}$$

The flow continuity equation for the rodless cavity of the asymmetric cylinder is

$$Q_1 = A_1 \frac{\mathrm{d}x_p}{\mathrm{d}t} + C_{im} p_1 + \frac{V_1}{\beta_e} \frac{\mathrm{d}p_1}{\mathrm{d}t}. \tag{27}$$

Assuming that the low-pressure cavity of the asymmetric cylinder is zero, the external load and friction forces are disregarded, and the force balance equation is simplified as follows:

$$A_1 p_1 = m_t \frac{\mathrm{d}x_p^2}{\mathrm{d}t} + B_p \frac{\mathrm{d}x_p}{\mathrm{d}t} + K x_p. \tag{28}$$

Combining Eqs. (26)–(28), the open-loop transfer function of the pump-controlled asymmetric cylinder system with positive motion is expressed as follows:

$$F_p = \frac{A_1 D_p w (m_t s^2 + B_p s + K)}{(m_t s^2 + B_p s + K)(\frac{V_1 s}{\beta_e} + K_{ip} + C_{im}) + A_1^2 s}. \tag{29}$$

Similarly, the open-loop transfer function of the pump-controlled asymmetric cylinder system in negative motion is expressed as follows:

$$F_p = \frac{A_2 D_p w (m_t s^2 + B_p s + K)}{(m_t s^2 + B_p s + K)(\frac{V_2 s}{\beta_e} + K_{ip} + C_{im}) + A_2^2 s}. \tag{30}$$

By comparing Eqs. (29) and (30), the unified expression for the open-loop transfer function of the pump-controlled asymmetric cylinder can be obtained as follows:

$$F_p = \frac{\frac{D_p w}{A_p}\left(m_t s^2 + B_p s + K\right)}{\left\{\begin{array}{l} \frac{m_t V}{\beta_e A_p^2} s^3 + \left(\frac{(C_{im}+K_{ip}) m_t}{A_p^2} + \frac{B_p V}{\beta_e A_p^2}\right) s^2 \\ + \left(1 + \frac{B_p (C_{im}+K_{ip}) m_t}{A_p^2} + \frac{KV}{A_p^2 \beta_e}\right) s + \frac{K(C_{im}+K_{ip})}{A_p^2} \end{array}\right\}}, \tag{31}$$

where, $C_t = C_{im} + K_{ip}$,

$$A_p = \begin{cases} A_1 & \dot{x}_p \geq 0 \\ A_2 & \dot{x}_p < 0 \end{cases},$$

$$V = (V_1 + V_2)/2.$$

After simplifying and integrating Eq. (31), the simplified transfer function of the pump-controlled asymmetric cylinder is expressed as follows:

$$F_p = \frac{\frac{D_p A_p \omega}{C_i}\left(\frac{s^2}{\omega_m} + \frac{2\xi_m}{\omega_m} s + 1\right)}{\left(\frac{s^2}{\omega_r} + 1\right)\left(\frac{s^2}{\omega_0} + \frac{2\xi_0}{\omega_0} s + 1\right)}, \tag{32}$$

where ω_m is the natural frequency of the load; ξ_m is the damping ratio of the load; ω_r is the ratio of the series coupling stiffness to the damping coefficient of the hydraulic spring and load spring; ω_0 is the natural frequency of the system composed of a hydraulic spring, load spring, and mass; ξ_0 is the damping ratio.

The parameters in Eq. (32) are expressed as follows:

$$\omega_m = \sqrt{\frac{K}{m_t}}, \tag{33}$$

$$\xi_m = \frac{B_p}{2} \sqrt{\frac{1}{K m_t}}, \tag{34}$$

$$\omega_r = \frac{C_t}{A_p^2 \left(\frac{1}{K} + \frac{1}{K_h}\right)}. \tag{35}$$

where K_h is the hydraulic spring stiffness.

$$K_h = \frac{\beta_e A_p^2}{V}, \tag{36}$$

$$\omega_0 = \omega_h \sqrt{\left(1 + \frac{K}{K_h}\right)}, \tag{37}$$

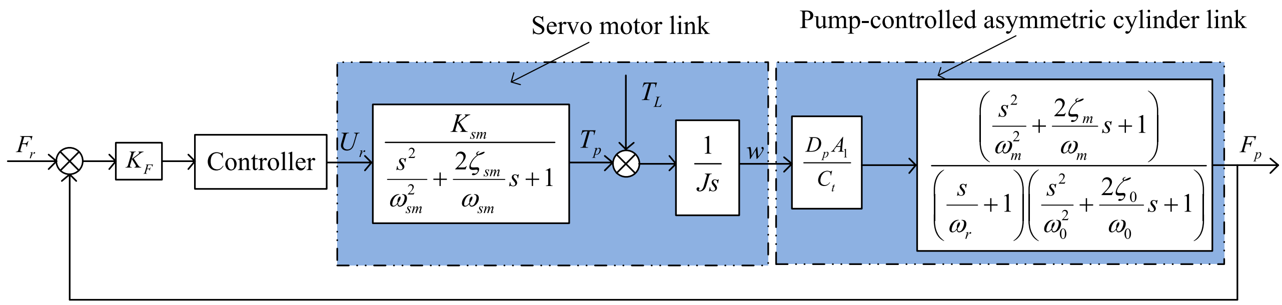

Figure 8 Transfer block diagram of pump-controlled asymmetric cylinder force control system

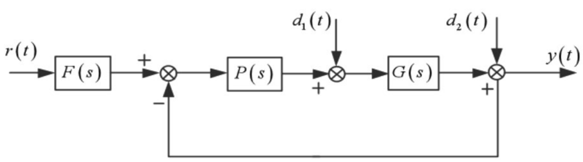

Figure 9 Control system block diagram of QFT controller

$$\xi_0 = \frac{1}{2\omega_h\sqrt{1+\frac{K}{K_h}}}\left(\frac{C_t\beta_e}{V}+\frac{B_p}{m_t}\right). \tag{38}$$

A control block diagram of the entire force control system after processing is shown in Figure 8.

3 Design of PCDS Force Controller

In this section, a force controller (QFT–DLOC) based on QFT and a DTO is proposed for the force control system of the pump control loop to improve the force control performance of the system.

3.1 Design of QFT Controller

3.1.1 QFT Controller

A QFT controller [28–30] is a robust controller based on the frequency domain. When the structure of a control object is uncertain and disturbance is present, a highly robust controller is to be designed based on the frequency domain theory of the control system. The design structure of the QFT controller is shown in Figure 9.

In Figure 9, $r(t)$ is the system input, and $y(t)$ is the system output, both of which can be measured independently. $G(s)$ is the controlled object exhibiting uncertainty, $d_1(s)$ and $d_2(s)$ are the unknown external disturbances of the system, and $P(s)$ is the controller, whose role is to ensure the robust performance of the system. $F(s)$ is a prefilter that guarantees the tracking performance of the system. By designing the appropriate transfer functions $P(s)$ and $F(s)$, the control system can satisfy the design performance index, and the bandwidth of the QFT controller can be minimized. The open-loop transfer function $L(s)$ and closed-loop transfer function $T_R(s)$ are subsequently defined for the control system structure shown in Figure 9.

$$L(s) = G(s)P(s), \tag{39}$$

$$T_R(s) = \frac{L(s)F(s)}{1+L(s)}, \tag{40}$$

$$T(s) = \frac{L(s)F(s)}{1+L(s)}. \tag{41}$$

Based on the structure of the control system shown in Figure 9, the controller $P(s)$ and prefilter $F(s)$ are designed to stabilize the closed-loop system and satisfy the frequency domain index. The typical frequency-domain indices are as follows:

(1) Index of robust stability

$$|T_1(j\omega)| = \left|\frac{P(j\omega)G(j\omega)}{1+P(j\omega)G(j\omega)}\right| \le \delta_1(\omega) = W_s. \tag{42}$$

(2) Anti-input disturbance index

$$|T_2(j\omega)| = \left|\frac{P(j\omega)}{1+P(j\omega)G(j\omega)}\right| \le \delta_2(\omega). \tag{43}$$

(3) Anti-output disturbance index

$$|T_3(j\omega)| = \left|\frac{1}{1+P(j\omega)G(j\omega)}\right| \le \delta_3(\omega). \tag{44}$$

(4) Tracking performance index

$$|T_l(j\omega)| \le \left|\frac{F(j\omega)P(j\omega)G(j\omega)}{1+P(j\omega)G(j\omega)}\right| \le |T_u(j\omega)|. \tag{45}$$

Table 1 Parameter variation range of force control simulation model

Parameter name	Initial value	Variation range
Equivalent proportional coefficient k_a	173.3	161.17–185.43185.
Natural frequency of servo motor ω_{sm}(rad/s)	141.60	131.69–151.51
Inherent damping ratio of servo motor ζ_{sm}	1.99	1.85–2.13
Natural frequency of load ω_m(rad/s)	158	146.94–169.06
Damping ratio of load ζ_m	0.75	0.70–0.8
Ratio of stiffness to damping coefficient of series coupling of hydraulic spring and load spring ω_r(rad/s)	1.67	1.55–1.79
Natural frequency of hydraulic spring and load spring and mass ω_0(rad/s)	1246	1158.78–1333.22
Damping ratio ζ_0	0.07	0.065–0.075

3.1.2 Determination of Parameter Uncertainty Set and System Template

The QFT controller was designed based on the transfer block diagram of the pump-controlled asymmetric cylinder force-control system shown in Figure 5, i.e., without considering the disturbance torque of the servo motor. The output force of the pump control loop F_p and the open-loop transfer function of the desired input F_r are expressed as follows:

$$G(s)=\frac{k_a\left(\frac{s^2}{\omega_m^2}+\frac{2\zeta_m}{\omega_m}s+1\right)}{s\left(\frac{s}{\omega_r}+1\right)\left(\frac{s^2}{\omega_0^2}+\frac{2\zeta_0}{\omega_0}s+1\right)\left(\frac{s^2}{\omega_{sm}^2}+\frac{2\zeta_{sm}}{\omega_{sm}}s+1\right)}, \tag{46}$$

where k_a is the equivalent proportionality coefficient.

By calculating the PCDS parameters, the formula of the open-loop transfer function (Eq. (46)) and the initial values (as shown in Table 1) are obtained. The equivalent proportionality coefficient is a typical control parameter. To improve the robustness of the system, the equivalent proportional coefficient must be adjusted dynamically based on the different operating conditions. In the sampling system, because of the nonlinear and high-order characteristics of the servo valve, after the servo valve becomes equivalent to the second-order oscillation link, it cannot fully reflect its actual dynamic characteristics. Consequently, the natural frequency and damping ratio of the servo valve are not constant because of the input signal and operating parameters. Therefore, ±7% of each parameter was specified as the uncertainty of the open-loop transfer function for force control, and the variation range of each parameter is shown in Table 1.

In the QFT controller, the object template [31, 32] is adopted to describe the uncertainty of objects at different frequency points. To obtain an appropriate object template while considering the frequency response of the system, a set of frequency points, i.e., $\omega=\{0.01,0.05,0.25,1,2,5,10,20,40\}$, was selected. At each frequency point, the amplitude range and the phase angle of the controlled object is displayed on the Nichols diagram, which forms the object template. The object template of the corresponding frequency points of the system was established using the quantitative feedback toolbox in MATLAB, as shown in Figure 10.

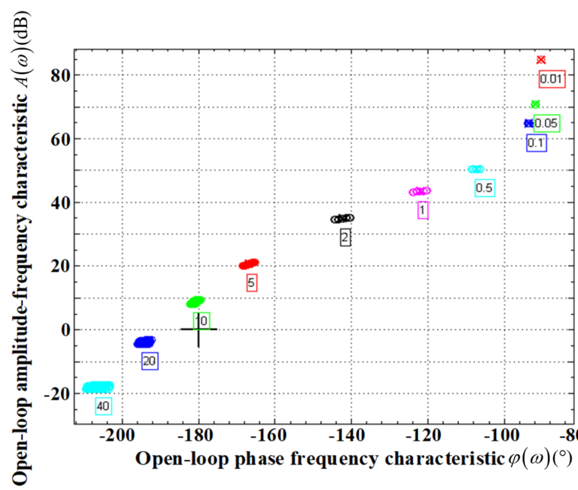

Figure 10 Object templates at different frequency points

Each point in Figure 10 represents the amplitude–frequency and phase–frequency characteristics of the system at different frequencies. Uncertain variations exist in the parameters, although the range is small.

3.1.3 System Index Requirement and Solution

In designing the QFT controller, the closed-loop robust stability and system tracking performance were regarded as the performance indices.

(1) Robust System Stability

When designing the controller in the frequency domain, the steady-state characteristics of the system can be determined based on the amplitude and phase

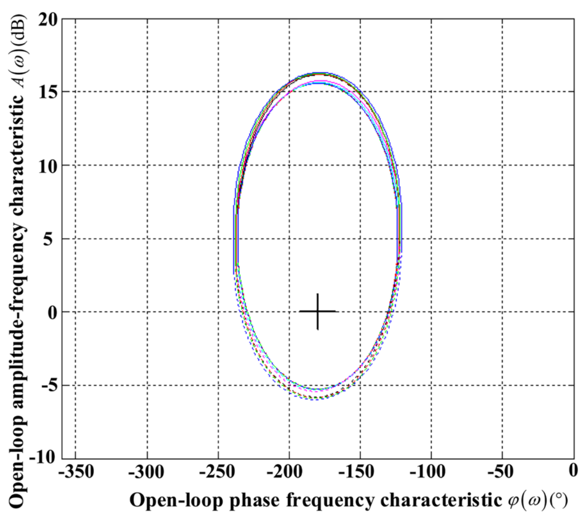

Figure 11 Robust stability boundary of pump control loop force control system

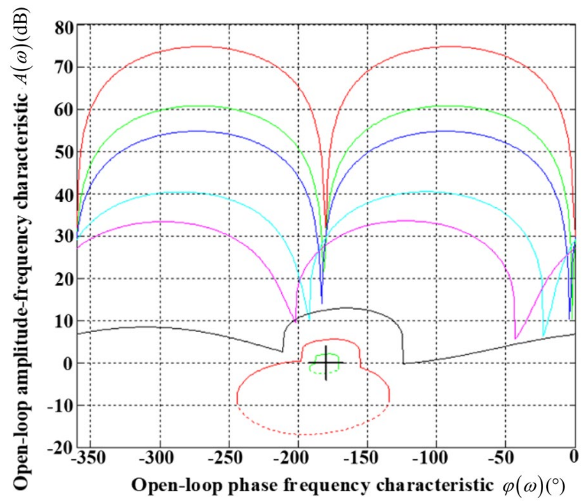

Figure 12 Trajectory tracking boundary

margins. The amplitude margin G_M, phase margin ϕ_M, and W_s are correlated as follows:

$$G_M \approx 20\log\left(\frac{W_s+1}{W_s}\right), \tag{47}$$

$$\Phi_M \approx \arcsin\left(\frac{1}{2W_s}\right). \tag{48}$$

To ensure the stability of the controlled system and that the resonance peak of the controlled system does not exceed 1.2, the amplitude and phase margins were as $G_M = 5.27$ dB and $\phi_M = 49.25$, respectively, based on calculations using Eqs. (47) and (48), respectively.

Based on the closed-loop robust stability constraint specified in Eq. (45), the robust stability boundary of the nominally controlled object of the pump control loop can be obtained using the QFT robust control toolbox.

As shown in Figure 11, when designing the QFT controller, provided that the Nichols diagram of the open-loop transfer function of the force control system is outside the robust stability boundary, the system can yield a robust stability index.

(2) Index of System Tracking Performance

To facilitate the design of the upper and lower bound functions of the system tracking performance, a typical second-order link was selected as the basic form of the system tracking performance, and the closed-loop transfer function of the second-order system is

$$W(s) = \frac{Y(s)}{R(s)} = \frac{\omega_n^2}{s^2 + 2\zeta\omega_n s + \omega_n^2}. \tag{49}$$

To stabilize the bandwidth of the PCDS to 3–10 Hz, the boundary functions were obtained when the natural frequencies were 3.18 and 9.55 Hz, and damping ratios were 0.9 and 0.6. The boundary functions were designed as follows:

$$T_u(s) = \frac{400}{s^2 + 36s + 400}, \tag{50}$$

$$T_1(s) = \frac{3600}{s^2 + 72s + 3600}. \tag{51}$$

The boundary functions shown in Eqs. (49) and (50) were adopted to obtain the trajectory tracking boundary of the nominally controlled object in the pump control loop through the QFT robust control toolbox, as shown in Figure 12.

As shown in Figure 12, when designing the QFT controller, provided that the point of the open-loop transfer function of the force control system on the Nichols diagram is outside (for the closed tracking performance boundary) or above (for the open tracking performance constraint boundary) the tracking performance boundary of each operating frequency, the system can satisfy the tracking performance index.

The two performance index requirements above were converted into a series of boundaries that constrain the open-loop frequency response curve in the Nichols diagram. The different constraint boundaries at various frequency points were integrated to form comprehensive performance boundaries, as shown in Figure 13.

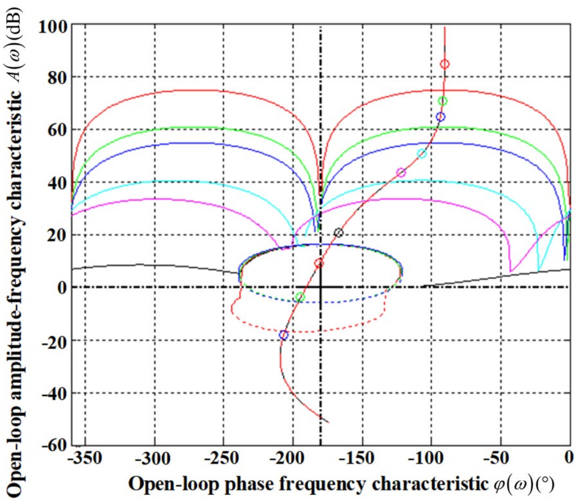

Figure 13 Open-loop frequency response of system before calibration.

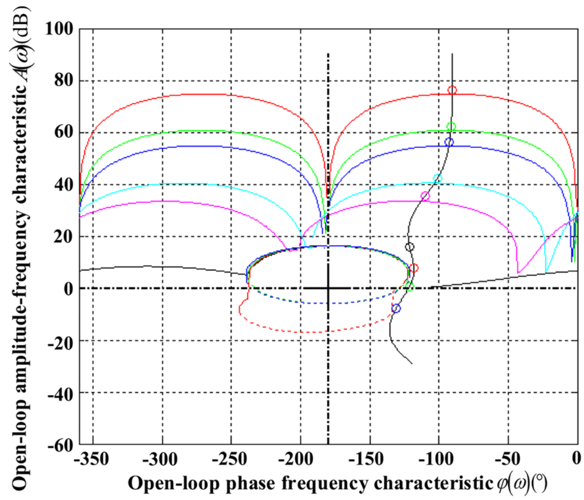

Figure 14 Open-loop frequency response of system after calibration

As shown in Figure 13, the open-loop Nichols curve of the system comprises a frequency range inside (for the closed constraint boundary) or below (for the open constraint boundary) the comprehensive performance constraint boundary area.

To satisfy the two performance indexes, the open-loop Nichols curve of the system was adjusted to outside or above the comprehensive performance constraint boundary area by adding zeros and poles as well as adjusting the gain, which is analogous to designing the controller's $P(s)$.

The design process is performed such that each frequency point is the closest possible to the comprehensive performance boundary, and the high-frequency gain decreases rapidly to suppress the effects of noise and the high-frequency resonance of the system at high frequencies. After drawing the composite index boundary on the Nichols diagram, the open-loop frequency response curve of the nominal object was plotted on the Nichols diagram using loop shaping. By continuously adjusting the zeros, poles, and controller gain, the response curve can be adjusted to above the performance index boundary at a low frequency, where its closer proximity to the boundary is desired. At this time, the bandwidth of the controller is minimum and does not intersect the stable boundary at high frequencies. When the response curve satisfies the boundary requirements, the zeros, poles, and gains used for adjustment constitute the designed controller. All characteristics are reflected in the Nichols diagram, and the process of adjusting the curve is equivalent to the process of obtaining the transfer function. The appropriate $P(s)$ is selected through simulation analysis, and the $P(s)$ of the QFT controller can be obtained as follows:

$$P(s)=\frac{0.38\left(\frac{s}{4.7}+1\right)}{\left(\frac{1}{300}s+1\right)\frac{1}{647.5^2}s+\frac{2\times0.707}{647.5}s+1}. \tag{52}$$

Figure 14 shows the open-loop frequency response of the system after calibration. As shown, the frequency range of the system open-loop Nichols curve is inside or below the comprehensive performance constraint boundary region.

3.2 Design of QFT–DTO Controller

In a PCDS, the disturbance torque generated by the load pressure of the gear pump affects the torque control performance of the servo motor, and the load pressure of the gear pump tends to fluctuate. In particular, when the system is disrupted by external locations, the pressure fluctuation is more intense, which adversely affects the force control accuracy and response speed of the system. When designing the QFT controller described in Section 2.1, the disturbance torque of the servo motor is disregarded to reduce the design difficulty. However, the load torque of the servo motor in the actual system is relatively high, particularly when controlling the HDU of a high-precision robot joint; as such, it should not be disregarded. Therefore, the disturbance torque was introduced into the force control system, and through appropriate control compensation, the disturbance rejection ability of the servo motor and the control precision of the force control system were improved.

The disturbance torque of the servo motor is a function of the gear pump's connection shaft angle and the load pressure of the gear pump. Additionally, it is affected

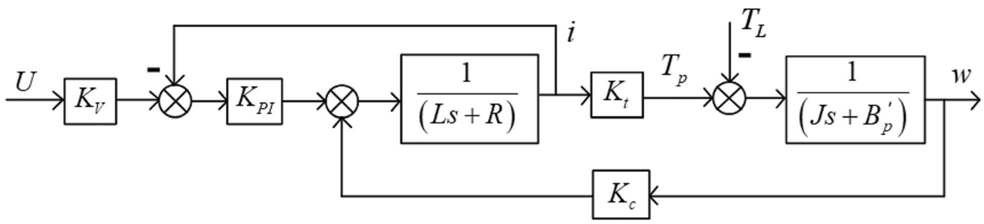

Figure 15 Transfer block diagram of the servo motor torque control system

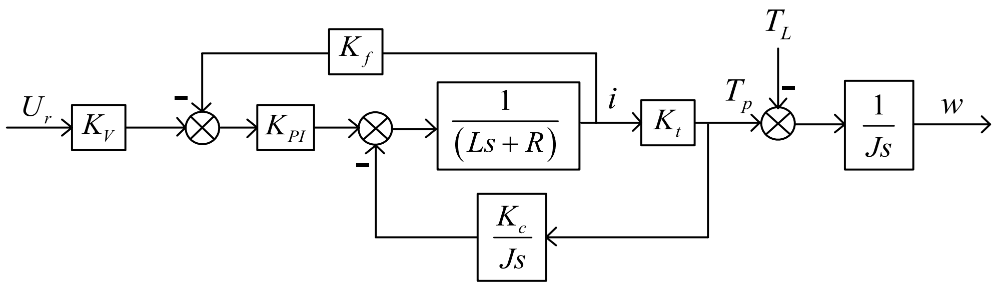

Figure 16 Transfer block diagram of torque control system of servo motor after deformation

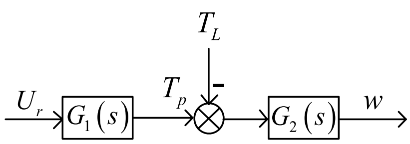

Figure 17 Simplified transfer block diagram of servo motor torque control

by factors such as friction resistance, which cannot be obtained using simple calculation theory. Furthermore, no experimental conditions are available for detecting the disturbance torque. Therefore, the disturbance torque of the servo motor must be measured indirectly via the DTO controller to design the appropriate compensation control experiments.

3.2.1 Design of Servo Motor DTO Controller

To obtain the disturbance torque of the servo motor more accurately, the disturbance torque of the servo motor was estimated using the DTO controller, and compensation was performed to eliminate the effect of the external torque disturbance on the control performance of the servo motor. The transfer function in Figure 8 was simplified to the product form of the basic transfer function link.

The transfer block diagram of the servo motor torque control system is shown in Figure 15.

To simplify the transfer function of the servo motor, the transfer block diagram of the torque control system of the servo motor was deformed, and the transfer block diagram of the torque control system of the servo motor after deformation was obtained, as shown in Figure 16.

A simplification of the transfer block diagram shown in Figure 16 yields the block diagram shown in Figure 17.

In Figure 17, $G_1(s)$ is the transfer function of the servo motor from the control voltage input to the torque output, and $G_2(s)$ is the transfer function of the servo motor from the torque input to the speed output. $G_1(s)$ and $G_2(s)$ are expressed as follows:

$$G_1(s) = \frac{K_V K_{PI} K_t}{LJs^2 + RJs + K_c K_t + K_{PI} K_f}, \tag{53}$$

$$G_2(s) = \frac{1}{Js}. \tag{54}$$

When designing the QFT controller, the disturbance torque of the servo motor was not considered. By disregarding the effect of the external disturbance torque, the open-loop transfer function of the servo motor can be obtained as follows:

$$\frac{w}{U_r} = G_1(s) \cdot G_2(s) = \frac{K_V K_{PI} K_t}{LJs^2 + RJs + K_c K_t + K_{PI} K_f} \cdot \frac{1}{Js}. \tag{55}$$

The open-loop transfer function of the servo motor was simplified to obtain the following expression:

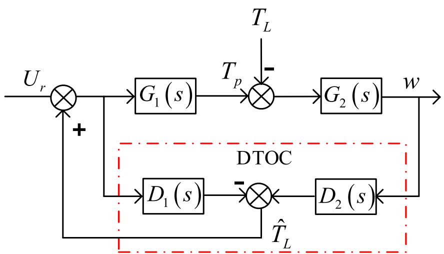

Figure 18 DTO control block diagram of servo motor

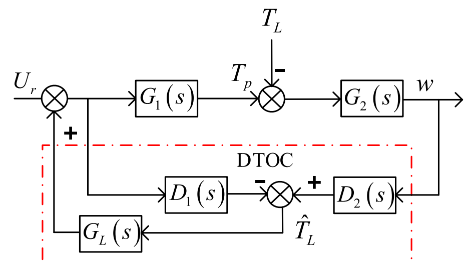

Figure 19 DTOC compensation control block diagram of service motor load

$$\frac{w}{U_r} = \frac{K_{sm}}{\frac{s^2}{\omega_{sm}^2} + \frac{2\zeta_{sm}}{\omega_{sm}}s + 1} \cdot \frac{1}{J_s}, \tag{56}$$

where K_{sm} is the open-loop gain of the servo motor (zero dimension), ω_{sm} the natural frequency of the servo motor, and ζ_{sm} the damping ratio of the servo motor (zero dimension).

Each parameter is expressed as follows:

$$K_{sm} = \frac{K_V K_{PI} K_t}{\left(K_c K_t + K_{PI} K_f\right)}, \tag{57}$$

$$\omega_m = \frac{K_c K_t + K_{PI} K_f}{LJ}, \tag{58}$$

$$\zeta_{sm} = \sqrt{\frac{R^2 J}{4L(K_c K_t + K_{PI} K_f)}}. \tag{59}$$

Based on the simplified torque control transfer block diagram of the servo motor, the DTO control block diagram of the servo motor can be obtained, as shown in Figure 18, where T_L is the disturbance torque observer.

In Figure 18, $G_1(s)$ is the transfer function from the control voltage input to the torque output of the servo motor, and $G_2(s)$ is the transfer function from the torque input to the speed output of the servo motor. Their expressions are shown in Eqs. (53) and (54) above.

Using the principle of disturbance invariance, the following were deduced: $D_1(s) = G_1(s)$ and $D_1(s) = 1/G_2(s)$. Based on Figure 18, the estimated value of the equivalent load torque can be obtained as follows:

$$\hat{T}_L = U_r G_1(s) - [U_r G_1(s) - T_L] G_2(s) G_2^{-1}(s) = T_L. \tag{60}$$

Therefore, the load torque of the servo motor can be accurately estimated using the method above.

Owing to the noise of the measured signal in the actual hydraulic control and the inability to establish an accurate mathematical model of the servo motor, the accuracy of the load torque observation decreased. Therefore, a low-pass filter, $G_L(s)$ was introduced after the observed value. And the DTOC compensation control block diagram of service motor load can be obtaned, as shown in Figure 19.

In Figure 19, $G_L(s)$ is critical to the design of the DTO, and a positive $G_L(s)/G_2(s)$ must be ensured, i.e., the relative order of $G_L(s)$ should not be less than that of $G_2(s)$. Additionally, the bandwidth design of $G_L(s)$ should comprehensively account for the robust stability and disturbance rejection suppression ability of the load observer.

As $G_2(s)=1/Js$, a low-pass filter with a third-order denominator and a first-order numerator was adopted, namely, $N=3$, $M=1$, and $k=0.1$. Based on $\alpha_k = N!/[(N-k)!k!], \alpha_0 = 1$ and $\alpha_1 = 3$ can be obtained. The low-pass filter is expressed as follows:

$$G_L(s) = \frac{\sum_{k=0}^{M} \alpha_k (\tau s)^k}{(\tau s + 1)^N} = \frac{\alpha_0 + \alpha_1 \tau s}{(\tau s + 1)^3} = \frac{3\tau s + 1}{\tau^3 s^3 + 3\tau^2 s^2 + 3\tau s + 1}, \tag{61}$$

where $\tau = 0.001$.

3.2.2 Design of QFT–DTO Controller

Combining the QFT controller described in Section 2.1 and the DTO controller described in this section, the QFT–DTO control block diagram of the pump control loop was obtained, as shown in Figure 20.

The model parameters and initial values used in the simulation of the pump–valve composite driving force control system are listed in Table 2.

4 Experiment

4.1 Operating Principle of PCDS Experimental Platform

To investigate the performance of the PCDS force control, a PCDS performance test platform was designed, as shown schematically in Figure 21.

The test platform for evaluating the PCDS force-control performance is shown in Figure 21. A counter

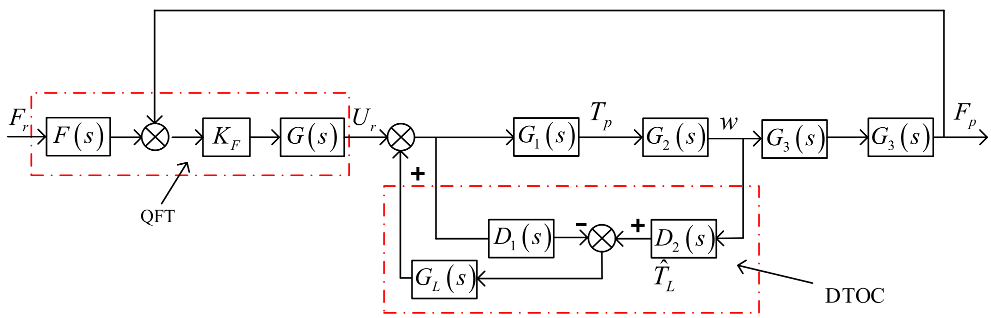

Figure 20 Control block diagram of QFT–DLO

Table 2 Simulation model parameters and initial values of pump–valve composite driving force control system

Parameter	Initialization value	Unit	Parameter	Initialization value	Unit
Voltage and current conversion coefficient of motor K_V	7.5	A/V	Current feedback coefficient K_f	1	–
Motor armature inductance L	3.28×10^{-4}	H	Motor armature winding resistance R	5.74×10^{-2}	Ω
Electromagnetic torque system of motor K_c	31.28	V/(rad/s)	Motor torque coefficient K_t	1.75	N·m/A
Inertia of servo motor shaft J_T	4.55×10^{-3}	(kg·m^2)	Viscous friction coefficient of servo motor B_T	0	N·m (rad/s)
Displacement of gear pump	1.05×10^{-6}	m^3/rad	Internal leakage coefficient of gear pump K_{ip}	1×10^{-12}	m^3/(s·Pa)
External leakage coefficient of gear pump K_{ep}	0	m^3/(s·Pa)	Asymmetric cylinder piston rodless cavity area A_1	6.62×10^{-4}	m^2
Rod cavity area of asymmetric cylinder piston A_2	6.62×10^{-4}	m^2	Asymmetric leakage coefficient outside cylinder C_{em}	0	m^3/(s·Pa)
Asymmetric in-cylinder leakage coefficient C_{im}	0	m^3/(s·Pa)	Total equivalent mass on asymmetric cylinder piston m_t	3.2	kg
Load stiffness of asymmetric cylinder K	5×10^{5}	N/m	Damping coefficient of asymmetric cylinder piston and load B_p	0	N/(m/s)
Coulomb friction force of asymmetric cylinder F_f	0	N	Load force exerting on asymmetric cylinder piston F_L	0	N
Connection volume between rodless cavity and gear pump V_{g1}	3.93×10^{-5}	m^3	Connecting volume of rod cavity and gear pump V_{g1}	3.93×10^{-5}	m^3
Operating chamber volume of gear pump V_{p1}	3.34×10^{-6}	m^3	Operating chamber volume of gear pump V_{p2}	3.34×10^{-6}	m^3
Total stroke of asymmetric cylinder L	0.075	m	Initial position of asymmetric cylinder L_0	0.035	m
Flow pressure coefficient of unidirectional valve		m^3/(s·Pa)	Initial pressure of booster tank P_{gp}	0.5	Pa
Initial volume of pressurized tank gas V_{gv}		m^3	Effective bulk elastic modulus of aviation hydraulic oil β_e	8×10^{8}	Pa
Gain of pressure sensor	5	V/bar	Aviation hydraulic oil density ρ	0.867×10^{3}	kg/m^3
Servo valve current gain K_{xv}	0.05	m/A	Servo valve power amplifier gain K_a	0.009	A/V
Damping ratio of servo valve ξ_{sv}	0.67	–	Natural frequency of servo valve ω_{sv}	502.4	rad/s

cylinder was adopted in the experimental platform. The section shown on the right is the PCDS, which was used to perform an experiment to evaluate the force control system of the HDU of the robot joint. The section shown on the left is the valve-controlled cylinder position control system, which was used to simulate the disturbance load during its movement. However, in the present experiment using the PCDS force control performance test platform, the servo valve pressure port P was connected to the volume of the two cavities of the asymmetric cylinder in the force control system, and the servo

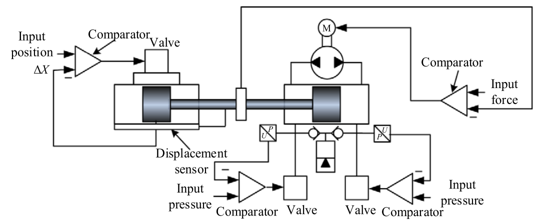

(a) Schematic diagram showing test platform for evaluating PCDS performance

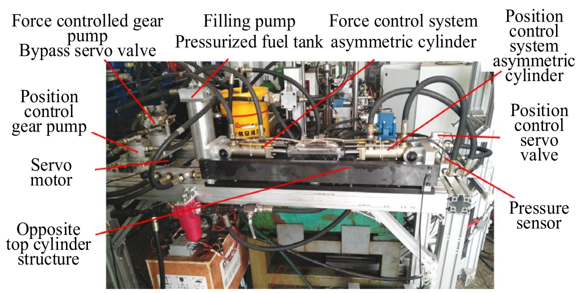

(b) Photograph of test platform for evaluating PCDS performance

Figure 21 Test platform for evaluating PCDS performance

Table 3 Experimental conditions of QFT-DTOC

Experimental condition	Sinusoidal input force		Sinusoidal disturbance position	
①	1000 N	0.5 Hz	–	–
②	2000 N	0.5 Hz	–	–
③	1000 N	0.5 Hz	8 mm	1 Hz
④	2000 N	0.5 Hz	8 mm	1 Hz

Table 4 One of QFT–DTOC performance indicators (%, indicated in two decimal digits)

Experimental condition	Performance index				
	Maximum force error (N)			Maximum elimination rate of force error (%)	
	PID	QFT	QFT–DTOC	QFT	QFT–DTOC
①	424.69	307.26	209.41	27.65	50.69
②	807.01	639.47	368.76	20.76	54.31
③	444.11	330.28	243.19	25.63	45.24
④	879.51	692.61	514.34	21.25	41.52

valve could only be used for oil discharge. The system was operated in the pump-drain valve compound drive mode.

4.2 Experimental Plan

The effectiveness of the QFT–DLO control method was evaluated. The valve control loop was controlled using the same PID parameters, and the specific experimental conditions are listed in Table 3.

4.3 Experimental Result

Table 4 lists the output force of the pump control loop in Figures 22, 23, 24, 25, where PID in the figure indicates the output force of the pump control loop with a simple PID controller, QFT indicates the output force of the pump control loop adopting the force control method based on QFT, and QFT–DTOC indicates the output force of the pump control loop adopting the force control method based on QFT and the DTO. To facilitate the analysis, Tables 4 and 5 are constructed based on the evaluation indices.

As shown in Figures 24, 25, Tables 3, and 5, when the force control system is provided with a sinusoidal force input and the disturbance position is based on the sinusoidal input, the QFT and DTO can improve the force-following accuracy. In particular, in the case involving load position disturbance, the DTO compensation effect was better. When the sinusoidal force-following signal of the system was 1000 N with a frequency of 0.5 Hz and the disturbance position featured an 8 mm amplitude with 1 Hz frequency, the maximum force error using PID control was 444.11 N, and the maximum force error of the force control system using QFT was 330.28 N. The maximum reduction rate of force error was approximately 25.63%. The maximum force error using the QFT–DTOC was 243.19 N, and the maximum force error elimination rate was approximately 45.24%, which was 19.61% less than the maximum force error rate using the QFT system only.

When only QFT was adopted in the system, the response curve of the force control system featured a certain phase angle lag, which is attributed to the following reason: Because the control method is designed based on the amplitude–frequency characteristic curve and the corresponding requirements for the phase angle is not satisfied when the QFT is adopted, a certain degree of phase angle lag is inevitable. However, the phase angle lag in the force control curve improved after using the QFT–DTOC. This is because by compensating for the disturbance load of the servo motor, the disturbance rejection ability of the servo motor and its response ability are improved. Hence, the response of the pump control loop is improved, and the issue regarding the phase angle lag is mitigated.

In general, under different experimental conditions, the QFT control method can improve the control accuracy by more than 20% compared with PID control, and

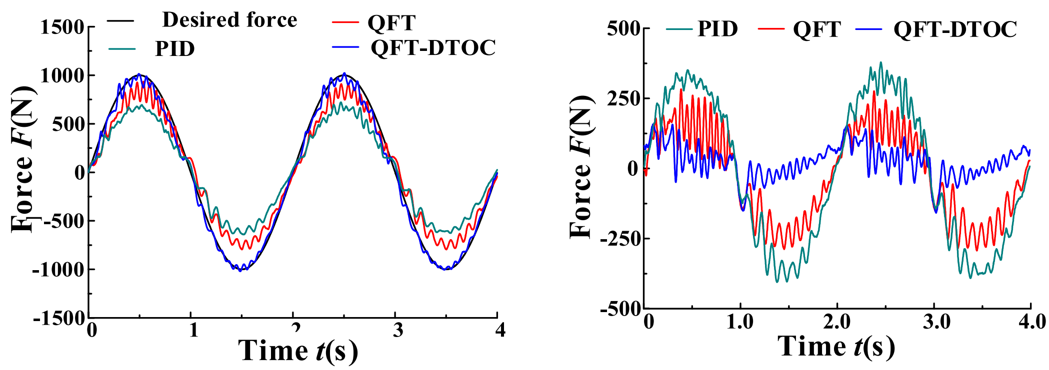

(a) Force control response curve **(b)** Force error curve

Figure 22 Force input exhibits 1000 N amplitude with 0.5 Hz frequency and no disturbance position

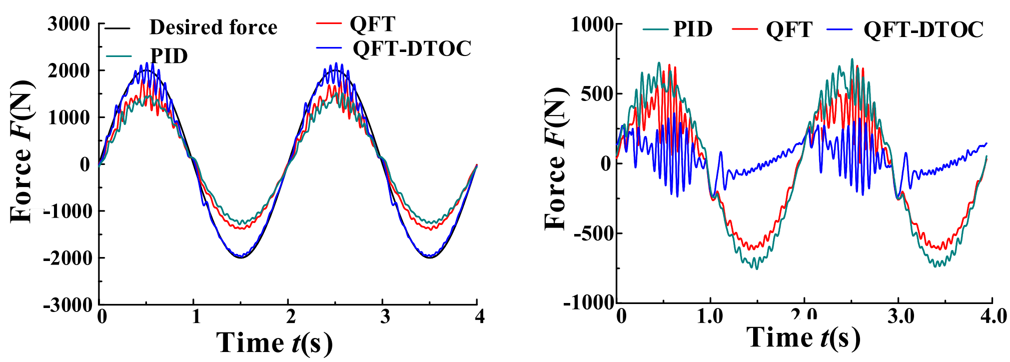

(a) Force control response curve **(b)** Force error curve

Figure 23 Force input exhibits 2000 N amplitude with 0.5 Hz frequency and no disturbance position

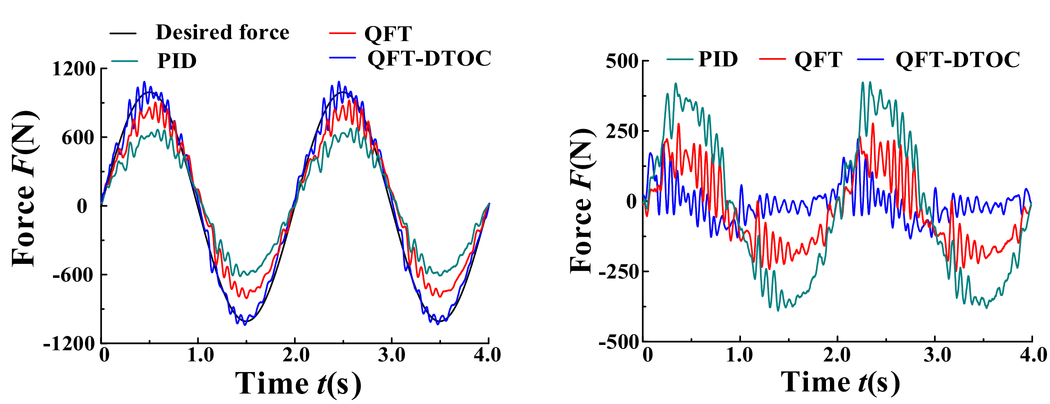

(a) Force control response curve **(b)** Force error curve

Figure 24 Force input exhibits 1000 N amplitude with 0.5 Hz frequency, and disturbance position exhibits 8 mm amplitude with 1 Hz frequency

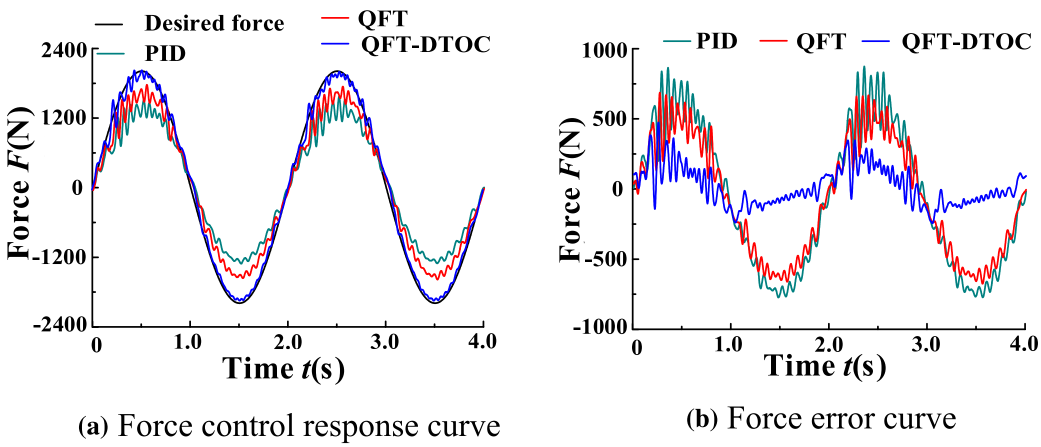

Figure 25 Force input exhibits 2000 N amplitude with 0.5 Hz frequency, and disturbance position exhibits 8 mm amplitude with 1 Hz frequency

Table 5 Another QFT–DLOC performance indicators (%, indicated in two decimal digits)

Experimental condition	Performance index				
	Average value of force error (N)			Average elimination rate of force error (%)	
	PID	QFT	QFT–DTO	QFT	QFT–DTO
①	242.47	168.25	75.46	30.61	68.88
②	451.64	346.38	168.78	23.34	62.63
③	239.96	169.87	55.84	29.21	76.73
④	443.82	331.84	111.43	25.23	74.89

the QFT–DTOC can improve the accuracy by more than 41% compared with PID control, thus improving the force control performance.

5 Conclusions

To satisfy the requirements of energy conservation, high precision, and fast response of the joint HDU of a legged robot combined with a pump–valve compound drive system, a mathematical model was established for each hydraulic component. Subsequently, the force control method was analyzed, and a force control method combining QFT and a DTO was devised. Before incorporating the QFT–DTO controller into the system, i.e., when only a simple PID controller was used, the force input signal was followed successfully, although the control performance was unsatisfactory. When the amplitude of the sine signal was increased, the system exhibited a significant following error. When only QFT was adopted in the system, the control accuracy was improved by more than 20% compared with that afforded by PID control. However, a phase angle lag was observed in the response curve of the force control system because QFT is a control method that is based on the amplitude–frequency characteristic curve, and it does not satisfy the corresponding requirements for the phase angle. Thus, a certain degree of phase-angle lag is inevitable. After incorporating the QFT–DTOC compensation controller designed in this study, the robustness and control accuracy of the force control system improved, and the following accuracy increased by more than 41%.

The PCDS test and experimental platform used in this study comprised an internal gear pump, which featured low-speed crawling, weak flow pressure pulsation, and other disadvantages, which resulted in significant fluctuations in the force control curve. Therefore, the low-speed characteristics of the internal gear pump should be investigated in the future such that relevant control compensation methods can be devised to reduce its effect on force control performance.

Authors' Contributions

KB proposed the experimental ideas, YW crafted the method design, XH verified the experimental data, CW performed data analysis, BY was responsible for experimental preparation, YL wrote the first draft, and XDK reviewed and revised the first draft. All authors have read and approved the final manuscript.

Funding

Supported by National Excellent Natural Science Foundation of China (Grant No. 52122503), Hebei Provincial Natural Science Foundation of China (Grant No. E2022203002), The Yanzhao's Young Scientist Project of China (Grant No. E2023203258), Science Research Project of Hebei Education Department of China (Grant No. BJK2022060), and Hebei Provincial Graduate Innovation Funding Project of China (Grant No. CXZZSS2022129).

Availability of Data and Materials

The datasets used or analyzed during the current study are available from the corresponding author upon reasonable request.

Declarations

Competing Interests

The authors declare that they have no conflicts of interest.

Received: 12 July 2021 Revised: 1 September 2022 Accepted: 21 December 2023
Published online: 20 March 2024

References

[1] J Y Zhai, Z B Song. Adaptive sliding mode trajectory tracking control for wheeled mobile robots. *International Journal of Control,* 2019, 92: 2255–2262.
[2] Q Y Liu, J G Zhao, H Y Zhu, et al. Review, classification and structural analysis of downhole robots: Core technology and prospects for application. *Robotics and Autonomous Systems*, 2019, 115: 104–120.
[3] O Y Kanner, N Rojas, L U Odhner. Adaptive legged robots through exactly constrained and non-redundant design. *IEEE Access,* 2017, 5: 11131–11141.
[4] C Gong, M J Travers, H C Astley, et al. Kinematic gait synthesis for snake robots. *International Journal of Robotics Research,* 2016, 35: 100–113.
[5] S Pan, L Shi, S Guo. A kinect-based real-time compressive tracking prototype system for amphibious spherical robots. *Sensors*, 2015, 15: 8232–8252.
[6] L. Lyu, Z. Chen and B. Yao. Advanced valves and pump coordinated hydraulic control design to simultaneously achieve high accuracy and high efficiency. *IEEE Transactions on Control Systems Technology*, 2021, 29: 236–248.
[7] B Chen, D R Gao, Y B Li, et al. Experimental analysis of spray behavior and lubrication performance under twin-fluid atomization. *Journal of Manufacturing Processes*, 2021, 61: 561–573.
[8] K X Ba, Y H Song, Y P Shi, et al. A novel one-dimensional force sensor calibration method to improve the contact force solution accuracy for legged robot. *Mechanism and Machine Theory*, 2022, 169: 104685.
[9] Y H Song, K X Ba, Y Wang, et al.Study on nonlinear dynamic behavior and stability of aviation pressure servo valve-controlled cylinder system. *Nonlinear Dynamics*, 2022, 108(4): 3077–3103.
[10] X M Yuan, W Q Wang, X Zhu, et al. Theory model of dynamic bulk modulus of aerated hydraulic fluid. *Chinese Journal of Mechanical Engineering*, 2022, 35:121.
[11] B Baigzadehnoe, Z Rahmani, A Khosravi, et al. On position/force tracking control problem of cooperative robot manipulators using adaptive fuzzy backstepping approach. *ISA Transactions,* 2017, 70: 432–446.
[12] L Xu, K Hao, L Chen, et al. Shared control of robot based on adaptive network-based fuzzy inference system. *2020 Chinese Automation Congress*, 2020, 1: 3612–3617.
[13] S Liu, Y Zhang and H Wang. Tracking control for nonlinear systems with input delay and dead-zone via adaptive fuzzy backstepping approach. *2021 13th International Conference on Advanced Computational Intelligence (ICACI)*, 2021, 1: 112–116.
[14] Y Xue, H Yu and X Liu. Improved fuzzy backstepping position tracking control for manipulator driven by PMSM, *2018 Chinese Automation Congress (CAC)*, 2018, 1: 3561–3565.
[15] D Won, W Kim, M Tomizuka. High gain observer based integral sliding mode control for position tracking of electro-hydraulic servo systems. *IEEE/ASME Transactions on Mechatronics,* 2017, 22: 2695–2704.
[16] M J Abbas, H S Zad, M Awais, et al. Robust sliding mode position control of electro-hydraulic servo system. *2019 International Conference on Electrical, Communication, and Computer Engineering (ICECCE)*, 2019, 1: 1–6.
[17] S Oh, K Kong. High-precision robust force control of a series elastic actuator. *IEEE/ASME Transactions on Mechatronics*, 2017, 22: 71–80.
[18] L Lyu, Z Chen, B Yao. Development of pump and valves combined hydraulic system for both high tracking precision and high energy efficiency. *IEEE Transactions on Industrial Electronics*, 2019, 66: 7189–7198.
[19] S M Lu, D J Li. Adaptive neural network control for nonlinear hydraulic servo-system with time-varying state constraints. *Complexity,* 2017, 2017: 1–11.
[20] Y J Liu, Q Zeng, L Liu, et al. An adaptive neural network controller for active suspension systems with hydraulic actuator. *IEEE Transactions on Systems, Man, and Cybernetics: Systems*, 2020, 50(12): 5351–5360.
[21] Z K Yao, J Y Yao, F Y Yao, et al. Model reference adaptive tracking control for hydraulic servo systems with nonlinear neural-networks. *ISA Transactions,* 2020, 100: 396–404.
[22] K Guo, M Li, W Shi and Y Pan. Adaptive tracking control of hydraulic systems with improved parameter convergence. *IEEE Transactions on Industrial Electronics*, 2022,69(7):7140–7150.
[23] Y Ye, C B Yin, Y Gong, et al. Position control of nonlinear hydraulic system using an improved PSO based PID controller. *Mechanical Systems & Signal Processing,* 2017, 83: 241–259.
[24] J Li, Y wang, Z Zhao, et al. Research on electro-hydraulic force servo control system based on specialist PID control strategy. *Journal of Computational and Theoretical Nanoscience*, 2017, 14: 341–346.
[25] Y Fan, J Shao, G Sun, et al. Improved beetle antennae search algorithm-based Lévy flight for tuning of PID controller in force control system. *Mathematical Problems in Engineering*, 2020, 22: 2020.
[26] K X Ba, Y H Song, C Y Wang, et al. A novel kinematics and statics correction algorithm of semi-cylindrical foot end structure for 3-DOF LHDS of legged robots. *Complex Intell. Syst,* 2022, 40747-022-00748-z.
[27] K X Ba, G L Ma, B Yu, et al. A nonlinear model-based variable impedance parameters control for position-based impedance control system of hydraulic drive unit. *International Journal of Control, Automation and Systems*, 2020, 18: 1806–1817.
[28] R Jeyasenthil, S B Choi. A new anti-windup compensator based on quantitative feedback theory for an uncertain linear system with input saturation. *Applied Sciences*, 2019, 9: 2958.
[29] G Su, J Sun, Z Li, et al. Data-driven anti-windup compensator synthesis for unknown linear systems with time delay. *International Journal of Systems Science,* 2021, 52(13): 2831–2844.
[30] M R Gharib, A Daneshvar. Quantitative-fuzzy controller design for multivariable systems with uncertainty. *International Journal of Control Automation and Systems*, 2019, 17: 1515–1523.
[31] W Shen, X Su, Y Pang, et al. Robust controller design for the excavator swing system under the active regulating common pressure rail. *Transactions of the Institute of Measurement and Control*, 2018, 40(11): 3323–3332.
[32] C Yan, J Song, N Sepehri. Synthesis of a MIMO QFT controller for hydraulic hybrid swing system of excavators. *International Journal of Fluid Power*, 2017, 19: 1–13.

Kaixian Ba born in 1989, is currently a professor at *Yanshan University, China*. He is currently a Ph.D. candidate superviser at *Hebei Provincial Key Laboratory of Heavy Machinery Fluid Power Transmission and Control, China*. He received his Ph.D. degree from *Yanshan University, China,* in 2018. His main research interests include electro-hydraulic servo control system and robot design and control.

Yuan Wang born in 1996, is currently a master candidate at *School of Mechanical Engineering, Yanshan University, China.* His main research interests include robot design and control.

Xiaolong He born in 1989, is currently a Ph.D. candidate at *School of Mechanical Engineering, Yanshan University, China*. His main research interests include robot design and control.

Chunyu Wang born in 1998, is currently a master candidate at *School of Mechanical Engineering, Yanshan University, China.* His main research interests include robot design and control.

Bin Yu born in 1985, is currently a professor at *Yanshan University, China*. He is currently a Ph.D. candidate superviser at *Hebei Provincial Key Laboratory of Heavy Machinery Fluid Power Transmission and Control, Qinhuangdao, China.*He received his Ph.D. degree from *Yanshan University, China,* in 2015. His main research interests include heavy machinery fluid transmission and control and robot design and control.

Yaliang Liu born in 1995, is a Ph.D. candidate at *Yanshan University, China*. His main research interests include electro-hydraulic servo control system and robot design and control.

Xiangdong Kong born in 1959, is currently a professor at *Yanshan University, China*. He serves as the Chairman of Fluid Transmission and Control Society which is a branch of Chinese Mechanical Engineering Society (CMES). His main research interests include electro-hydraulic servo control system, heavy machinery fluid transmission and control and robot design and control.